

WM-99-118

# Nonperturbative evaluation of the few-body states for scalar $\chi^2\phi$ interaction

Çetin Savkli<sup>1</sup>

*Department of Physics, College of William and Mary, Williamsburg, VA, 23187*

## Abstract

A knowledge of nonperturbative propagators is often needed when the standard perturbative methods are not applicable. An example of this is the bound state problem in field theory. While a nonperturbative result is valuable by itself, it is also an important guide for those who work on developing phenomenological models for the nonperturbative problem. The Feynman-Schwinger representation approach provides a convenient framework for calculating nonperturbative propagators. In this paper we provide an algorithm for computing 1,2, and 3 body bound states with the inclusion of all self energies, vertex corrections, ladder and crossed ladder exchanges. The calculation is done in the quenched approximation by ignoring the matter loops. We provide simulation results for 1,2 and 3-body states.

PACS codes: 12.38.-t

Keywords: Nonperturbative, Monte-Carlo, bound states, Feynman-Schwinger representation

---

<sup>1</sup>csavkli@physics.wm.edu

# Program Summary

*Title of the Programs:* phi3

*Computer:* Sun 19

*Operating system:* Unix

*Programming language used:* FORTRAN 77

*Peripherals used:* Laser Printer

*Number of lines in distributed program:* 1510

*Keywords:* Nonperturbative, bound states, Feynman-Schwinger representation, Monte-Carlo, numerical evaluation.

*Nature of physical problem:*

The program provided here evaluates the mass and distribution probabilities of the fully interacting n-body propagator ( $n \leq 3$ ) for scalar  $\chi^2\phi$  interaction in 3+1 dimensions. The evaluation takes into account *all self energy, vertex dressing, and exchange interaction* contributions except those involving matter loops (the quenched approximation).

*Method of solution:*

The Feynman-Schwinger representation approach is used to express the field theoretical Green's function in terms of a quantum mechanical path integral. The resultant expression is evaluated using a Monte-Carlo simulation.

*Restrictions of the program:*

Only  $n = 1, 2$ , and 3 body propagators are considered. The extension to  $n \geq 4$  requires straightforward modifications in the program.

*Typical running time:*

About 1 day for the 1-body propagator with the self energy.

# LONG WRITE-UP

## 1 Introduction

In nuclear physics one is often faced by problems that require nonperturbative methods. The best known example is the problem of bound states. Even if the underlying theory may have a small coupling constant (such as in QED), and therefore allows the use of perturbation theory in general, the treatment of bound states are inherently nonperturbative. The n-body bound state is defined by the pole of the interacting n-body propagator. A perturbative approximation of n-body propagator does not produce the bound state pole location. Therefore it is essential that reliable nonperturbative methods that take all orders of interaction into account are developed. For this reason, numerous nonperturbative methods have been developed and successfully used in the literature. Some of the best known examples are lattice gauge theory [1] (LGT), and relativistic bound state equations [2, 3, 4].

In a recent paper [5] we (along with authors J. Tjon, and F. Gross) have discussed yet another method known as the Feynman-Schwinger representation(FSR). The basic idea in the FSR approach [5, 6, 7, 8] is to integrate out all fields at the expense of introducing quantum mechanical path integrals over the *trajectories of particles*. Replacing the path integrals over fields with path integrals over trajectories has an enormous computational advantage. The advantage is due to the fact that the path integration over trajectories involves a variation of *lines* rather than *fields in a volume*. Therefore the degrees of freedom is considerably fewer. The FSR approach differs from the LGT in that it utilizes a space-time continuum, therefore maintaining the Poincare symmetry. On the other hand it should be pointed out that the FSR approach is not without its drawbacks. In particular, how to extend the FSR approach to include fermions is not known. In the past researchers [8, 9, 10] have attacked the fermion problem using various approximations. An *exact* result involving fermions is an important problem and requires further study.

While being able to calculate a nonperturbative result by itself is interesting, an additional motivation in studying the FSR approach is to determine which subsets of diagrams give the dominant contribution to the n-body propagator. This is particularly important in determining what kind of approximations are reasonable within the context of bound state equations. An

example of how the FSR results can be used to compare different nonperturbative approximation schemes was presented in Refs [5, 11]. In those works the emphasis was on the development of the formalism and application to the 1 and 2-body propagators. In Ref [11], The FSR prediction for the 1-body mass in Scalar QED was compared by the rainbow-Dyson-Schwinger equation prediction. It was found [11] that while the FSR approach provides a real mass pole for all coupling strengths, the Dyson-Schwinger equation provides a complex mass pole beyond a critical coupling strength. Furthermore it was found that, for Scalar QED in 0+1 dimension, the vertex corrections to the exchange interaction do not contribute to the 2-body binding energy [11]. These examples demonstrate the potential usefulness of the FSR approach. The knowledge about the nonperturbative propagators and vertices provided by the FSR is valuable as an input in testing and improving the modeling of other nonperturbative approaches such as Dyson-Schwinger equations. [12, 13]

The two and three-body bound state sectors provide possibilities for the application of the FSR formalism. In particular it is important to see how various bound state equations (such as Bethe-Salpeter, Gross (spectator), Blankenbekler-Sugar, Equal-time, and nonrelativistic) compare with the quenched FSR results. Applications of the FSR approach to 2 and 3 body states with comparisons to various bound state equation results in  $\chi^2\phi$  theory is currently under study and will be presented in a separate article. [19]

In this paper we present a complete numerical algorithm for the evaluation of  $n$ -body masses ( $n \leq 3$ ) and distribution probabilities for scalar  $\chi^2\phi$  interaction in 3+1 dimensions. By providing this algorithm we intend to facilitate the comparison of various nonperturbative methods with the exact quenched results in  $\chi^2\phi$  theory. The organization of the paper is as follows: In the next section we present a brief summary of the FSR formalism. In the third section, using various 1, 2, and 3-body cases as examples, we discuss how results are obtained. And in the fourth section we explain the components of the program.

## 2 The Feynman-Schwinger representation for scalar fields

We consider the theory of charged scalar particles  $\chi$  of mass  $m$  interacting through the exchange of a neutral scalar particle  $\phi$  of mass  $\mu$ . The Euclidean Lagrangian for this theory is given by

$$\mathcal{L}_E = \chi^* [m^2 - \partial^2 + g\phi] \chi + \frac{1}{2} \phi (\mu^2 - \partial^2) \phi. \quad (1)$$

The two body Green's function for the transition from the initial state  $\Phi_i = \chi^*(x)\chi(\bar{x})$  to final state  $\Phi_f = \chi^*(y)\chi(\bar{y})$  is given by

$$G(y, \bar{y}|x, \bar{x}) = N \int \mathcal{D}\chi^* \int \mathcal{D}\chi \int \mathcal{D}\phi \Phi_f^* \Phi_i e^{-S_E}. \quad (2)$$

The final result for the two-body propagator involves a quantum mechanical path integral that sums up contributions coming from all possible *trajectories* of *particles*

$$G = - \int_0^\infty ds \int_0^\infty d\bar{s} \int (\mathcal{D}z)_{xy} \int (\mathcal{D}\bar{z})_{\bar{x}\bar{y}} e^{-S[Z]}, \quad (3)$$

where  $S[Z]$  is given by

$$S[Z] \equiv -iK[z, s] - iK[\bar{z}, \bar{s}] + V_0[z, s] + 2V_{12}[z, \bar{z}, s, \bar{s}] + V_0[\bar{z}, \bar{s}]. \quad (4)$$

where

$$K[z, s] = (m^2 + i\epsilon)s - \frac{1}{4s} \int_0^1 d\tau \frac{dz_\mu(\tau)}{d\tau} \frac{dz^\mu(\tau)}{d\tau}, \quad (5)$$

$$V_0[z, s] = \frac{g^2}{2} s^2 \int_0^1 d\tau \int_0^1 d\tau' \Delta(z(\tau) - z(\tau'), \mu), \quad (6)$$

$$V_{12}[z, \bar{z}, s, \bar{s}] = \frac{g^2}{2} s \bar{s} \int_0^1 d\tau \int_0^1 d\bar{\tau} \Delta(z(\tau) - \bar{z}(\bar{\tau}), \mu). \quad (7)$$

Here the  $V_0[z, s]$  term represents the self energy contribution, while the  $V_{12}[z, \bar{z}, s, \bar{s}]$  term represents the exchange interaction (Fig. 1). The interaction kernel  $\Delta(x)$  is defined by

$$\Delta(x, \mu) = \int \frac{d^4 p}{(2\pi)^4} \frac{e^{ip \cdot x}}{p^2 + \mu^2} = \frac{\mu}{4\pi^2|x|} K_1(\mu|x|). \quad (8)$$

While we present expressions for the 2-body case, generalization to an arbitrary n-body system is trivial. The bound state spectrum can be determined from the spectral decomposition of the two body Green's function

$$G(T) = \sum_{n=0}^{\infty} c_n e^{-m_n T}, \quad (9)$$

where  $T$  is defined as the average time between the initial and final states

$$T \equiv \frac{1}{2}(y_4 + \bar{y}_4 - x_4 - \bar{x}_4). \quad (10)$$

In the limit of large  $T$ , the ground state mass is given by

$$m_0 = \lim_{T \rightarrow \infty} -\frac{d}{dT} \ln[G(T)] = \frac{\int \mathcal{D}Z S'[Z] e^{-S[Z]}}{\int \mathcal{D}Z e^{-S[Z]}}, \quad (11)$$

While this result in principle is correct, the convergence to the asymptotic mass is slow due to the continuum contribution. The spectrum of the particle involves the mass pole and a cut beyond this pole representing the continuum contribution. Assuming that the constituents of the bound state are restricted to be at equal times in the initial and final states, the Green's function can be written as a function of time  $T$ , total displacement  $\mathbf{R}$ , and relative coordinate  $\mathbf{r}$ ,  $G(T, \mathbf{R}, \mathbf{r})$ .<sup>1</sup>

In order to eliminate the contribution of continuum states, introduce the Fourier transform,

$$\tilde{G}(T, \mathbf{P}, \mathbf{p}) = \int d^3\mathbf{R} d^3\mathbf{r} e^{i\mathbf{P}\cdot\mathbf{R} + i\mathbf{p}\cdot\mathbf{r}} G(T, \mathbf{R}, \mathbf{r}) \quad (12)$$

where  $\mathbf{P}$  is the CM momentum, and  $\mathbf{p}$  is the relative momentum between particles. Setting both  $\mathbf{P} = \mathbf{p} = 0$  one has

$$\tilde{G}(T, 0, 0) = \int d^3\mathbf{R} d^3\mathbf{r} G(T, \mathbf{R}, \mathbf{r}), \quad (13)$$

which eliminates the contribution of the continuum and projects out the s-wave state. While an integration over  $\mathbf{r}$  is not necessary for the elimination of the continuum contribution, it is useful in eliminating the contribution of states with nonzero orbital angular momentum.

---

<sup>1</sup>Dependence on the initial relative final coordinate  $\mathbf{r}_0$  is implicit.

While the result for the Green's function Eq. 3 is exact in the quenched approximation, due to its oscillatory behavior it is not appropriate for Monte-Carlo simulation. In Ref. [5] it was shown that one can perform a Wick rotation in variable  $s$  to avoid these oscillations. In the limit  $g^2 \rightarrow 0$  the dominant contribution to the integral in Eq. (3) can be shown, by using the saddle point method, to come from

$$s = is_0 = i \frac{T}{2m}. \quad (14)$$

Since the large  $s$  values do not contribute to the integral even without the interaction term, it is a good approximation to suppress the  $g^2$  term at large  $s$  values. While this suppression is done it is important that the integrand is not modified in the region of dominant contribution  $s \sim is_0$ . This can be achieved by scaling the  $s$  variable, *in the interaction term only*, by

$$s \rightarrow \frac{s}{R(s, s_0)}, \quad (15)$$

where

$$R(s, s_0) \equiv 1 - (s - is_0)^2 / \Gamma^2. \quad (16)$$

In the free case, ( $g^2 = 0$ ), the width  $W$  of the region of dominant  $s$  contribution goes as

$$W = \sqrt{\frac{T}{2m^3}}. \quad (17)$$

Therefore, in the free case the dominant contribution to the  $s$  integral comes from  $i(s_0 - W) < s < i(s_0 + W)$ . This claim is supported by the Monte-Carlo simulation results. In Fig. 2 we present the results for  $s$ -distributions for two different coupling strengths for time  $T = 40$ , and  $m = 1$  GeV. According to the estimate given above Eq. (17), for  $g = 0$ , the dominant contribution to the  $s$ -distribution comes from the region  $15.53 < s < 24.47$  which is in agreement with the result presented in Fig. 2. In order to ensure that the scaling given in Eq. (15) does not make a significant change in the region of dominant contribution,  $\Gamma$  should be chosen such that

$$\Gamma \geq W \quad (18)$$

As one increases the coupling strength, the value of  $s_0$  deviates from its free value. Therefore, in general,  $s_0$  has to be defined self consistently by monitoring the peak of the  $s$  distribution. In Figure 2 we display the  $s$ -distribution

for two different coupling strengths. It is seen that as the coupling strength is increased the peak of the s-distribution moves towards higher s values. In general the peak of the distribution can be parameterized as

$$s_0 = C \frac{T}{2m}. \quad (19)$$

The dependence of  $C$  on coupling strength  $g^2$  is determined self consistently. In Fig. 3  $C$ , which gives the location of the stationary point through Eq. (19), is plotted as a function of the coupling strength  $g^2$ . According to Fig. 3, it is not possible to find a self consistent stationary point beyond the critical coupling strength of  $g^2 = 31$  GeV $^2$ . A similar critical behavior was also observed in Refs. [14] within the context of a variational approach.

The insensitivity of the dressed mass to the width  $\Gamma$  has been investigated [5] and found that a choice of  $\Gamma^2 = 2W^2$  was satisfactorily large. Results presented here employ the same value of  $\Gamma$ .

Prescription given by Eqs. (15), and (16) enables one to perform a Wick rotation in variable  $s$  to obtain a finite and non-oscillatory expression for the fully interacting two-body propagator:

$$G = \int_0^\infty ds \int_0^\infty d\bar{s} \int (\mathcal{D}z)_{xy} \int (\mathcal{D}\bar{z})_{\bar{x}\bar{y}} \times \exp \left[ -K[z, s] - K[\bar{z}, \bar{s}] + V_0[z, s_r] + V_0[\bar{z}, \bar{s}_r] + 2V_{12}[z, \bar{z}, s_r, \bar{s}_r] \right], \quad (20)$$

where

$$s_r \equiv \frac{s}{R(s, s_0)}. \quad (21)$$

The path integral is discretized using

$$(\mathcal{D})_{xy} \rightarrow (N/4\pi s)^{2N} \prod_{i=1}^{N-1} \int d^4 z_i, \quad (22)$$

where the s-dependence is critical in obtaining the correct normalization. Note that the integration over the final coordinates is not included in this expression.

The discretized versions of kinetic and interaction terms are given by

$$K[z, s] \rightarrow (m^2 + i\epsilon)s - \frac{N}{4s} \sum_{i=1}^N (z_i - z_{i-1})^2, \quad (23)$$

$$V_0[z, s] \rightarrow \frac{g^2 s^2}{2N^2} \sum_{i,j=1}^N \Delta\left(\frac{1}{2}(z_i + z_{i-1} - z_j - z_{j-1}), \mu\right), \quad (24)$$

$$V_{12}[z, \bar{z}, s, \bar{s}] \rightarrow \frac{g^2 s \bar{s}}{2N^2} \sum_{i,j=1}^N \Delta\left(\frac{1}{2}(z_i + z_{i-1} - \bar{z}_j - \bar{z}_{j-1}), \mu\right). \quad (25)$$

We next address the regularization of the ultraviolet (short distance) singularities. The ultraviolet singularity in the kernel  $\Delta(x, \mu)$  Eq. (8) can be regularized using a Pauli-Villars regularization prescription. In order to do this one replaces the kernel

$$\Delta(x, \mu) \longrightarrow \Delta(x, \mu) - \Delta(x, \alpha\mu), \quad (26)$$

where  $\alpha$  is in principle a large constant. The ultraviolet singularity in the interaction is of the type

$$\int dz z \Delta(z, \mu). \quad (27)$$

At short distances the kernel  $\Delta(z, \mu)$  goes as  $1/z^2$ . Therefore, the self energy calculation involves a logarithmic type singularity. The Pauli-Villars regularization takes care of this singularity. The Pauli-Villars regularization is particularly convenient for Monte-Carlo simulations since it only involves a modification of the kernel. In order to achieve an efficient convergence in numerical simulations we use a rather small cut-off parameter  $\alpha = 3$ . This choice leads to a less singular kernel. The value of  $\alpha$  can be increased arbitrarily at the cost additional computational time. It should be noted that while we employ a Pauli-Villars regularization throughout this paper, in general, the bound state problem *without* self energies *does not* have any UV singularities. UV singularities are only associated with the self energies of the particles. After this brief summary of the formalism, in the next section we present some of the results and discuss the details of the algorithm.

### 3 Running the code: applications

The Monte-Carlo simulation starts by choosing an initial configuration for the trajectories of the particles. The choice of the initial trajectory is arbitrary (except at the end points). In Fig. 4 the evolution of the action as a function of number of updates for two different initial conditions is displayed. Starting

with a random initial trajectory is analogous to a high temperature system and the thermalization (reaching to the ground state) takes a long time (about 1000 updates). However if one starts by a classical free trajectory, the initial configuration is analogous to a frozen system without any fluctuations and the thermalization results in an increase of the action. However asymptotically both results should converge as shown in Fig. 4. We usually start with an orderly system and disregard the first 1000 updates. Step sizes of the random walker in configuration space and in s-space should be chosen such that the average acceptance rate of Monte-Carlo updates are about % 50. In each run we typically make 500000 updates of trajectories. In order to reduce the statistical errors runs must be repeated (usually more than 10 times) using different random number seeds. The correlation function  $X(n)$  of sampled configurations in each run is defined as

$$X(n) \equiv \frac{\langle m(i)m(i+n) \rangle - \langle m \rangle^2}{\langle m \rangle^2}, \quad (28)$$

where  $m(i)$  is the mass measurement at the  $i$ 'th update. The correlation function  $X(n)$  measures how the information about a given configuration is lost as a function of the number of updates  $n$ . In Figure 5 we show the correlation function for the 1-body problem. According to Fig. 5 the number of updates necessary for the correlation between sampled trajectories to vanish is around  $n = 1000$ . The number of configurations sampled in our simulations, which is around 500000, is well above the correlation length 1000, thereby insuring that uncorrelated trajectories are sampled during the Monte-Carlo integration.

The time  $T$  required to reach to the asymptotic limit increases as  $g^2$  increases. For  $g^2 = 25$  the asymptotic value of the mass, given by Eq. (11), is obtained around  $mT = 40$ . In particular for the result shown in Fig. 6, as  $g^2$  ranged from  $g^2 = 0$  GeV $^2$  to  $g^2 = 31$  GeV $^2$  the asymptotic time values used were increased from  $mT = 35$  to  $mT = 45$ . As time  $T$  is increased the number of steps  $N$  should also be proportionally increased so that the step size of the particle trajectory remains the same. As one increases the coupling strength  $g^2$ , trajectories of the particles deviate from the classical trajectory to a greater degree. This increase in fluctuations requires that one uses a higher  $N$  value. The number of steps  $N$  particles take between the initial and final coordinates is typically chosen to be  $35 < N < 45$ .

In Fig. 6 the  $g^2$  dependence of the one-body dressed mass is presented. 1-body masses presented here are lower than those in [5]. This is due to the fact that in that work  $C$  was assumed to be approximately 1. However it was subsequently realized that  $C$  deviates from 1 significantly (see Fig. 3) as coupling strength is increased, and a self consistent determination of  $C$  is important to pin down the critical point. According to Fig. 3 there is no self consistent stationary point Eq. (19) beyond the critical coupling strength  $g^2 = 31 \text{ GeV}^2$ , and the 1-body dressed mass becomes unstable for  $g^2 > 31 \text{ GeV}^2$  (Fig. 6).

Next two applications involve the two and three-body bound states of equal mass particles. While the algorithm provided is capable to take into account all self energy and vertex dressing corrections to the bound state, in the bound state applications provided here the self energy contributions of particles were not taken into account. This is controlled by a switch in the input file (see Table 4.1 for input options). In Fig. 7 the  $g^2$  dependence of the two-body bound state mass is presented. Beyond the critical coupling strength of  $g^2 = 100 \text{ GeV}^2$  the 2-body mass becomes unstable. During the Monte-Carlo simulation the radial distributions of particles are stored in histograms. In general for an  $n$ -body bound state there are  $n(n-1)/2$  relative distances. Since the particles are assumed to have equal time coordinates in the final state, essentially the relative distance is equal to the spatial distance. Let  $r_{ij} = |r_i - r_j|$  be the distance between particles  $i$  and  $j$ . In this case the histogram  $P_{ij}(r_{ij})$  stores the number of final state configurations sampled in the interval  $(r_{ij} - \delta/2, r_{ij} + \delta/2)$ , where  $\delta$  is the bin size. The range of  $r_{ij}$  values is specified in the program using

$$0 < r_{ij} < \frac{20}{m_i + m_j} \text{ Fermi.} \quad (29)$$

The choice of range is arbitrary as long as a reasonably smooth histogram is produced. The number of bins in each histogram is chosen to be 100. Therefore for two particles of mass 1 GeV, the maximum radius to be histogrammed is 10 Fermi; and the size of each bin is given by  $\delta = 0.1 \text{ Fermi}$ . In Fig. 8 we present the projection of the radial probability distribution onto a two-dimensional surface. The two-body probability distribution, presented in Fig. 8, shows the result for  $g^2 = 25 \text{ GeV}^2$ . Notice that the probability distribution vanishes at the origin. This is due to the phase space factor  $4\pi r^2$ . In order to be able to compare the probability distribution with a

wave function the phase space factor should be factored out. In general the radial wave function *amplitude*  $\Psi(r)$  is given by:

$$|\Psi(r)| = \sqrt{\frac{P(r)}{4\pi r^2}} \quad (30)$$

The normalization of the probability distribution histogram presented in Fig. 9 is arbitrarily fixed such that the maximum entry is equal to 1.

In generating the surface plot (Fig. 8), it is assumed that one of the particles is fixed at the origin. The amplitude of the surface gives the probability of finding the second particle at a distance  $r$ . While the surface plot for a two-body bound state is not necessary for a visual understanding of the bound state structure, the three-body bound state demands a three dimensional plot. In the three-body case there are three relative coordinates. In order to be able to plot the three-body probability distribution we fix the location of two of the particles along the y axis, and calculate the probability of finding the third particle in an arbitrary distance from two fixed particles. In Fig. 10 we represent the probability distribution of the third particle for a given fixed configuration of the first and second particles. Assume that the fixed particles are particle 1 and particle 2. The probability distribution of the third particle is given by

$$P_3(|\mathbf{r}_3|) \equiv P_{13}(|\mathbf{r}_3 - \mathbf{r}_1|)P_{23}(|\mathbf{r}_3 - \mathbf{r}_2|) \quad (31)$$

Probability distribution  $P_3(|\mathbf{r}_3|)$  includes the phase space contribution. Therefore  $P_3(|\mathbf{r}_3|)$  represents the probability of finding the third particle in a ring shown in Fig. 11. For example in the first plot of Fig. 10 two fixed particles are very close to each other such that the third particle sees them as a point particle. Therefore the probability distribution of the first plot of Fig. 10 is very similar to the two-body distribution given in Fig. 8. However as the fixed particles are separated from each other the third particle starts having a nonzero probability of being in between the two fixed particles (second and third plots of Fig. 10). Eventually when the two fixed particles are kept away from each other the third particle has a nonzero probability distribution only at the origin (the last plot shown in Fig. 10). In Fig. 12 the *two-body* distribution function  $P_{12}$  in a three-body system is shown. All of these plots were produced with three equal particles of mass 1 GeV, and the coupling strength of  $g^2 = 64$  GeV<sup>2</sup>.

## 4 Program details

In this section we discuss the details of the program. We start by providing the tables of input parameters 4.1 and arrays 4.2 and then summarize the components of the program.

### 4.1 Description of Input parameters

SIG = 1 GeV	Arbitrary momentum scale
IPAR(I)	I=1,2,3, Particles present (0=n, 1=y)
IEXCH(I,I)	I=1,2,3, Self Interactions (0=n, 1=y)
IEXCH(I,J)	(I, J) = (1, 2), (1, 3), (2, 3) Exch. Int. (0=n, 1=y)
QM(I)	Mass of particle I
G	The coupling strength
XMU	The exchange mass $\mu$
ALPHA	The Pauli-Villars mass ratio: $m_{pv} = \alpha \mu$
BETA = 1	The width of $R(s, s_0) \equiv 1 - \beta(s - iC\hat{s}_0)^2/T^\gamma$
GAMMA = 1	The T dependence of the width.
C	The peak location of the s distribution $s=C\hat{s}_0$ . C is determined self-consistently.
N	Number of steps along the trajectory
NSMPL	# of sampled trajectories in MC integration
NVOID	No. of uncounted samples for initial thermalization
ZSTEP	Max. step size of the random walker in coord. space
SSTEP	Max. step size of the random walker in $s$ space
EPSA	The short distance(UV) cut-off for preventing explicit occurrence of 1/0.0 type of singularity. This is not a regulator however. The UV regularization is done using Pauli-Villars subtraction
IDUM	The seed of the random number generator
Z(I,0,J)	Initial coordinates of particle I=1,2,3
Z(I,N,J)	Final coordinates of particle I=1,2,3
IWRTA,IWRTM	Action, mass to be stored in file ? (0=n, 1=y)
INTOUT	Integrate over final coordinates ?

## 4.2 Arrays

QM(3)	Particle masses
IPAR(3)	Determines which particles are present.
Z(3,0:400,4)	The trajectories of particles
ZNEW(3,0:400,4)	The updated trajectories of particles
SMAX(3)	The maximum value of s value to be histogrammed. (not an integration cut-off)
RMAX(3,3)	The maximum relative distance between particles to be histogrammed. (not an integration cut-off)
SHIST(3,200)	Histogram of s values
RHIST(3,3,200)	Histogram of relative distances between particles
SUMK(3)	Kinetic energies of particles
SUMV(3,3)	Potential energies of particles: SUMV(I,I): self energy of the I'th particle, SUMV(I,J): the exchange energy between I'th and J'th particles.
SUMKN(3)	Updated kinetic energies
SUMVN(3,3)	Updated potential energies

## 4.3 Main Program

The main program starts by calling the INPUT subroutine. This subroutine reads input parameters described in Table 4.1. Next, subroutine XINTGR is called to perform the Monte-Carlo simulation. In the following the role of each subroutine and function is explained.

## 4.4 Subroutine INPUT

In this subroutine 12 input parameters are read. In addition to reading these parameters, histograms for the radial and s distributions, and initial trajectories of the particles are initialized. Initialization of trajectories is done using the classical free trajectories of particles.

## 4.5 Subroutine XINTGR

This subroutine *controls* basic steps of the Monte-Carlo sampling process. First, the kinetic and the potential sums corresponding to the initial trajectories of particles are calculated by calling the XSUMS subroutine. Next step is the thermalization process. In order to reach thermalization the configuration of trajectories are updated NVOID times by calling the UPDATE subroutine. First NVOID updates are not used in the actual calculation of the bound state mass or the probability distribution. After the thermalization the sampling is done for NSMPL times. The results for the  $s$  values and the relative distances of particles are histogrammed. Finally the bound state mass is calculated.

## 4.6 Subroutine UPDATE

This subroutine is responsible for updating the current configuration of trajectories. Each coordinate and  $s$  parameter is updated once. Samplings are done according to distribution

$$e^{-S[z]} \quad (32)$$

distribution. If the ratio  $r$ ,

$$r = e^{-(S[z'] - S[z])}, \quad (33)$$

is larger than 1 updates are always accepted. When  $r < 1$  the update is accepted with a probability of  $r$ .

## 4.7 Subroutine XSUMS

This subroutine calculates kinetic and potential sums before the configuration updates start. Since calculation of the kinetic and potential sums is a costly operation, after every update we calculate the *shift* in the sums.

## 4.8 Subroutine ACTION

This subroutine calculates the action using known values of kinetic and potential sums. The action is stored in a file to monitor the thermalization. ( See Fig. 4 ).

## 4.9 Subroutine UPDSUM

Since calculation of the kinetic and potential sums is a costly operation, after every update we calculate the *shift* in the sums. Using this shift sums are updated.

## 4.10 Function XDERIV

This subroutine calculates the derivative operator  $S'[Z]$  Eq. (11) which gives the mass of the bound state.

## 4.11 Function DELTA, DELTAP

These subroutine calculate, respectively, the interaction kernel Eq. (8) and its time derivative.

## 4.12 Function DLARAN

This is a random number generator obtained from LAPACK package at Netlib. [17] DLARAN returns a random real number from a uniform (0,1) distribution. In the actual implementation of the program we have used a Numerical Recipes random number generator (ran2). However for copyright reasons here we provide this alternative random number generator.

## 4.13 Functions BESK0, BESK1, KZEONE

BESK0 and BESK1 are modified bessel functions  $K_0(x)$  and  $K_1(x)$  which are needed in calculation of the interaction kernel and its derivative. BESK0 and BESK1 call KZEONE subroutine [18]. KZEONE subroutine returns real and imaginary parts of  $e^x K_0(x)$  and  $e^x K_1(x)$ . The KZEONE subroutine is considerably slower than the Numerical Recipes subroutines for modified bessel functions. For copyright reasons we provide KZEONE rather than the Numerical Recipes subroutines for the modified bessel functions.

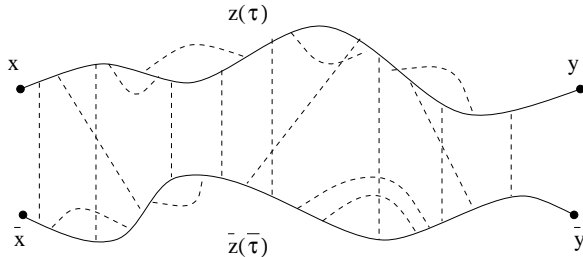


Figure 1: A sample trajectory of each particle along with various interactions are shown. Except the matter loops all self energy, exchange energy and vertex dressings are included.

## 5 Conclusions

In this paper, using the Feynman-Schwinger representation, we have presented an algorithm that calculates 1,2,3 body masses and distribution probabilities in the quenched approximation for  $\chi^2\phi$  theory in 3+1 dimension. The FSR approach provides an efficient method to calculate nonperturbative propagators. In this work we have presented results of applications to the 1, 2 and 3 body states. A detailed comparison of quenched bound state results of the FSR approach with the bound state equation predictions is under study and will be presented in a separate physics article [19]. It is hoped that, through comparison, this simple and rigorous nonperturbative method will enhance our understanding of various nonperturbative bound state models and approximations.

### Acknowledgements

We are grateful to F. Gross, and J. Tjon for discussions. The support of the DOE through grant No. DE-FG02-97ER41032 is gratefully acknowledged. The Thomas Jefferson National Accelerator Facility is gratefully acknowledged for warm hospitality and for providing computer resources.

## References

[1] H. J. Rothe, '*Lattice Gauge Theory*', World Scientific 1992.

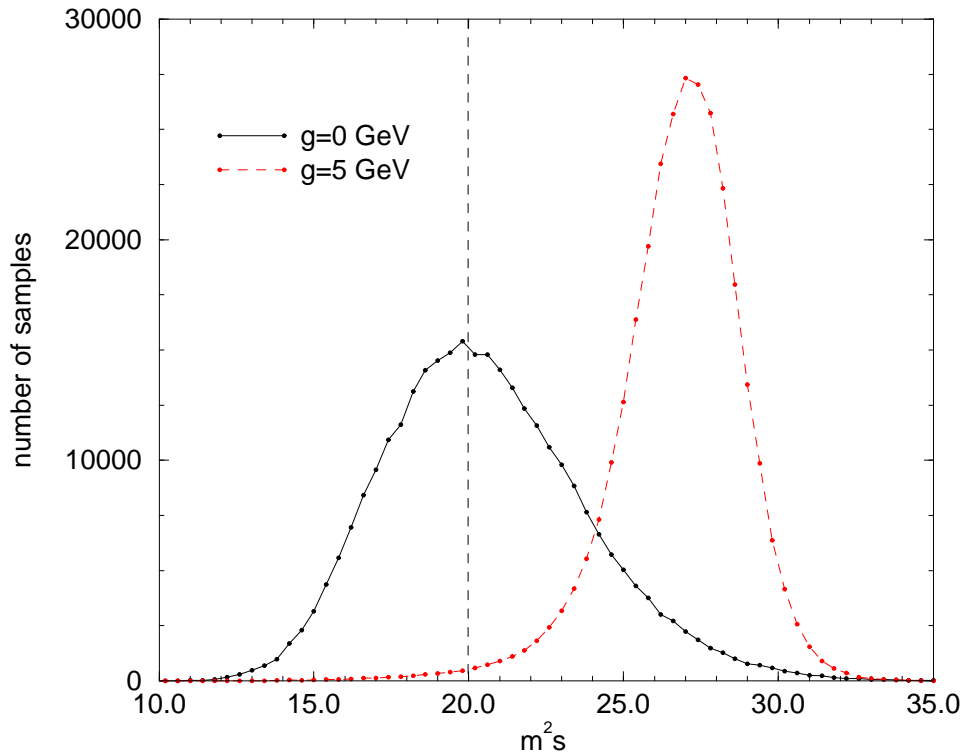


Figure 2: The sample distribution of Feynman parameter  $s$  is shown for two different coupling strengths. The peak of the distribution moves from the classical value  $T/2m$  as the coupling strength is increased.

- [2] N. Nakanishi, Prog. Theor. Phys. Suppl. **43** (1969) 1; *ibid* **95**, 1 (1988).
- [3] P. C. Tiemeijer, J. A. Tjon, Phys. Rev. C **48** (1993); *ibid* C **49**, 494 (1994).
- [4] F. Gross, Phys. Rev. C **26**, 2203 (1982).
- [5] Ç. Şavkli J. Tjon, F. Gross, Phys. Rev. C **60** 055210 (1999), Erratum-*ibid*.C61:069901,2000
- [6] Yu. A. Simonov and J. A. Tjon, Ann. Phys. **228**, 1 (1993).

- [7] T. Nieuwenhuis and J. A. Tjon, Phys. Rev. Lett. **77**, 814 (1996).
- [8] N. Brambilla, A. Vairo, Phys. Rev D. **56**, 1445 (1997).
- [9] Y. A. Simonov, Nucl. Phys. B **307** 512 (1988).
- [10] Y. A. Simonov, Nucl. Phys. B **324** 67 (1989).
- [11] Ç. Şavkli, F. Gross, J. Tjon, hep-ph/9907445, JLAB-THY-99-18, WM-99-110
- [12] C. D. Roberts and A. G. Williams, Prog. Part. Nucl. Phys. **33**, 477 (1994).
- [13] Ç. Şavkli, F. Tabakin, Nucl. Phys. A **628**, 645 (1998).
- [14] R. Rosenfelder, A.W. Schreiber, Phys. Rev. D **53** 3337, 1996; Phys. Rev. D**53**, 3354, 1996.
- [15] F. Gross and J. Milana, Phys. Rev. D **43**, 2401 (1991); **45**, 969 (1992); **50**, 3332 (1994).
- [16] T. Nieuwenhuis, PhD-thesis, University of Utrecht (1995), unpublished.
- [17] LAPACK auxiliary routine, Univ. of Tennessee, Univ. of California Berkeley, NAG Ltd., Courant Institute, Argonne National Lab, and Rice University, February 29, 1992
- [18] Algorithm 484 Collected Algorithms from NetLib, Appeared in COMM. ACM, VOL. 17, NO. 09, P. 524.
- [19] Ç. Şavkli, F. Gross, J. Tjon, in preparation.

## 6 Test run INPUT

1.0	SIG (GeV)
1 0 0	IPAR(1), (2), (3)
1 0 0	IEXCH(1,1)(2,2)(3,3)
0 0 0	IEXCH(1,2)(1,3)(2,3)
1.0	QM(1)
1.0	QM(2)
1.0	QM(3)
2.0	G
0.15	XMU
3.0	ALPHA
0.5	BETA
1.0	GAMMA
1.0	C
35	N
500000	NSMPL
5000	NVOID
2.1	ZSTEP
4.5	SSTEP
1.0D-4	EPSA
1	IDUM
0. 0. 0. 0.	Initial coordinates
1. 1. 0. 0.	“
-1. 1. 0. 0.	“
0. 0. 0. 35.	Final coordinates
1. 1. 0. 35.	“
-1. 1. 0. 35.	“
0 0	IWRPA, IWRPM
1	INTOUT

## 7 OUTPUT

SIG	1.0 GeV
Particles present	1 0 0
Self interactions	1 0 0
Exchange " 1-2	0
" " 1-3	0
" " 2-3	0
QM(1)	1. GeV
QM(2)	1. GeV
QM(3)	1. GeV
G	2. GeV
XMU	0.15 GeV
ALPHA	3.
BETA	0.5
GAMMA	1.
C	1.
N	35
NSMPL	500000
NVOID	5000
ZSTEP	2.1 1/GeV
SSTEP	4.5 1/GeV <sup>2</sup>
EPSA	0.10E-03 GeV <sup>-1</sup>
IDUM	1
Initial coordinates:	0 0 0 0 GeV <sup>-1</sup> 1 1 0 0 GeV <sup>-1</sup> -1 1 0 0 GeV <sup>-1</sup>
Final coordinates:	0 0 0 35 GeV <sup>-1</sup> 1 1 0 35 GeV <sup>-1</sup> -1 1 0 35 GeV <sup>-1</sup>
INTOUT	1
z update %	50.33
s update %	53.63
Bound state mass	0.97±0.001 GeV

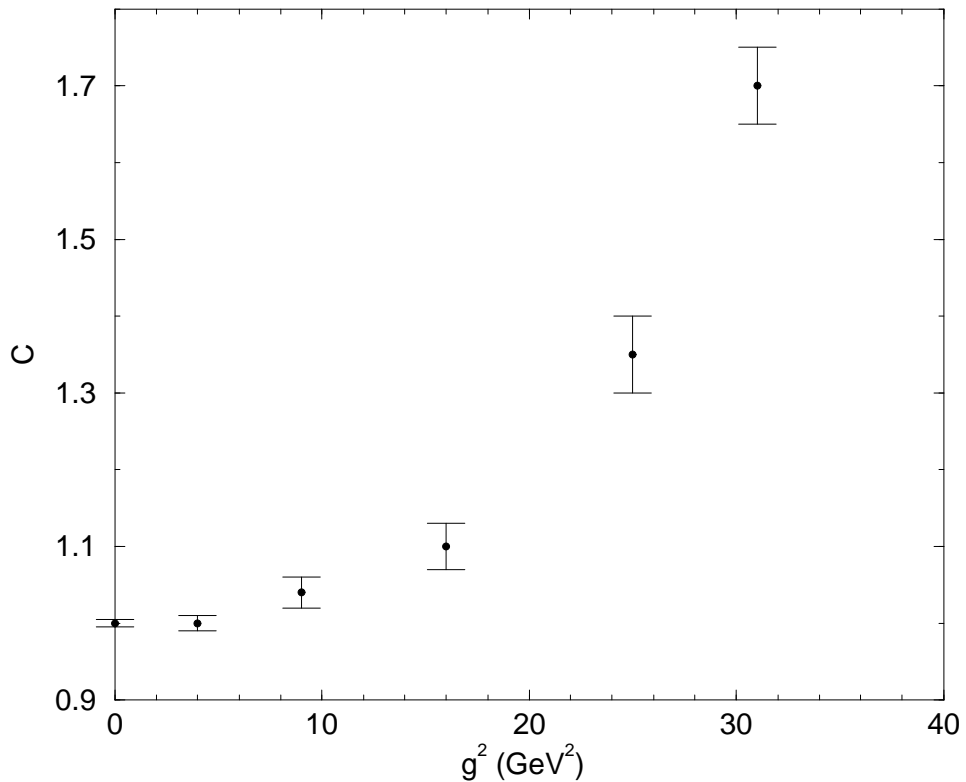


Figure 3: The dependence of the peak of the s-distribution on the coupling strength is shown. The peak location is given by  $s_0 = CT/2m$ . Beyond the critical coupling strength of  $g^2 = 31\text{GeV}^2$  a self consistent determination of  $C$  is not possible. Therefore beyond the critical coupling strength 1-body mass becomes unstable.

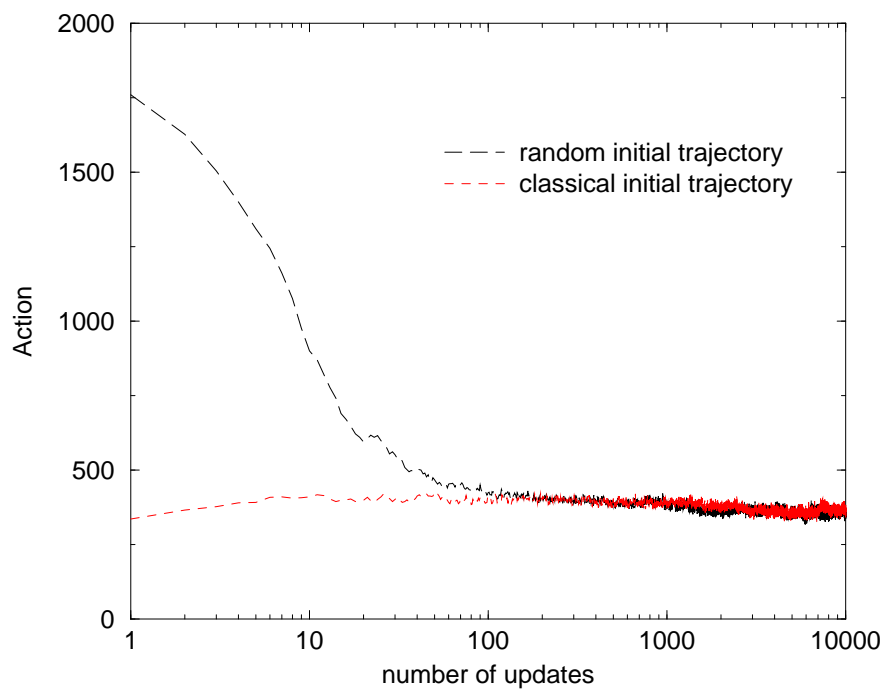


Figure 4: The thermalization for two different initial configurations is shown. Irrespective of the initial conditions the action approaches to an asymptotic limit. The first 1000 updates are ignored.

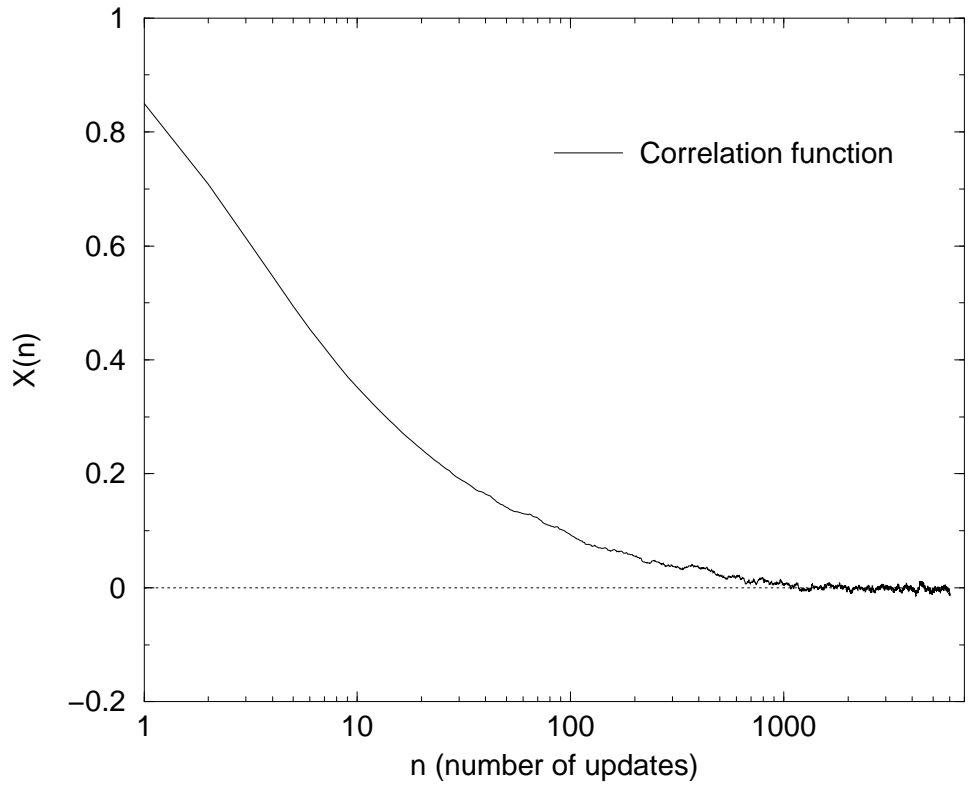


Figure 5: Here we present the correlation function for the 1-body simulation. The number of updates necessary for the correlation to vanish is around  $n = 1000$ . The typical number of updates performed in our simulations, which is around 500000, is well above the correlation length, thereby insuring that statistically uncorrelated configurations are sampled.

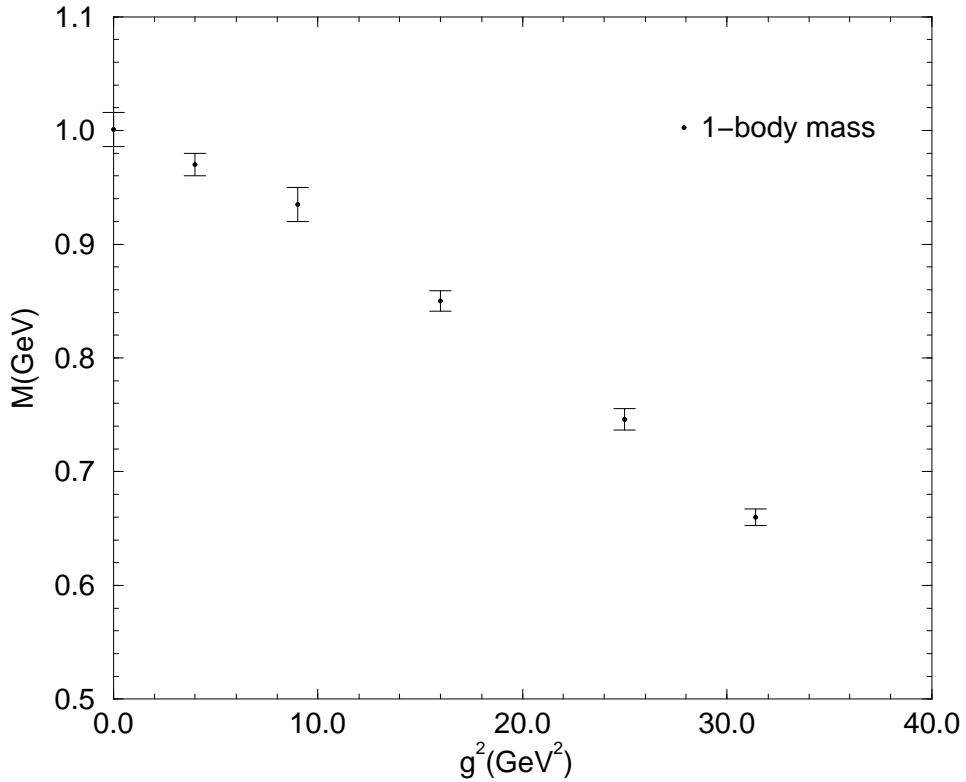


Figure 6: The coupling constant dependence of the 1-body dressed mass is shown. The asymptotic time value  $T$  used to obtain these mass values increase as  $g$  increases. While at  $g^2 = 0 \text{ GeV}^2$   $mT = 35$  is sufficient, at  $g^2 = 31 \text{ GeV}^2$   $mT = 45$  is needed. The peak of the  $s$  distribution was self consistently determined. Beyond the critical coupling strength of  $g^2 = 31 \text{ GeV}^2$  the 1-body mass becomes unstable.

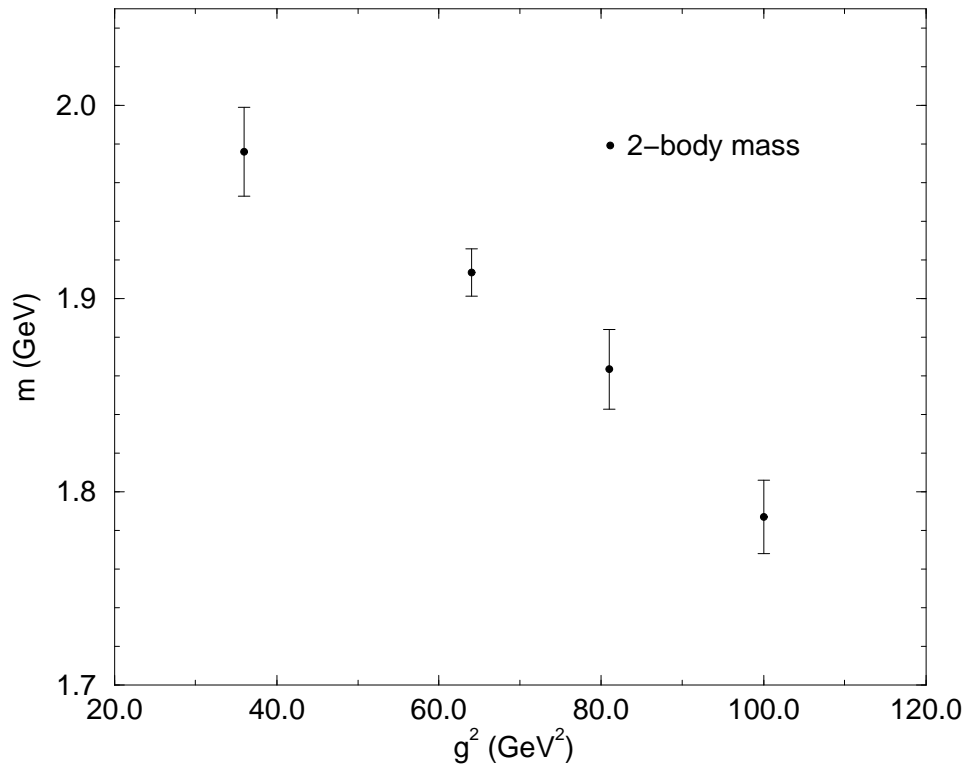


Figure 7: The coupling constant dependence of the 2-body bound state mass is shown. Beyond the critical coupling strength of  $g^2 = 100$  GeV $^2$  the 2-body mass becomes unstable.

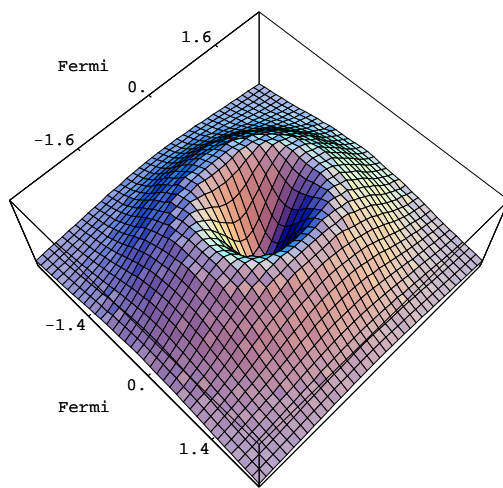


Figure 8: The 2-body probability distribution when the 1st particles is at the origin. The vanishing of probability at the origin is due to the phase space factor Eq. (30).

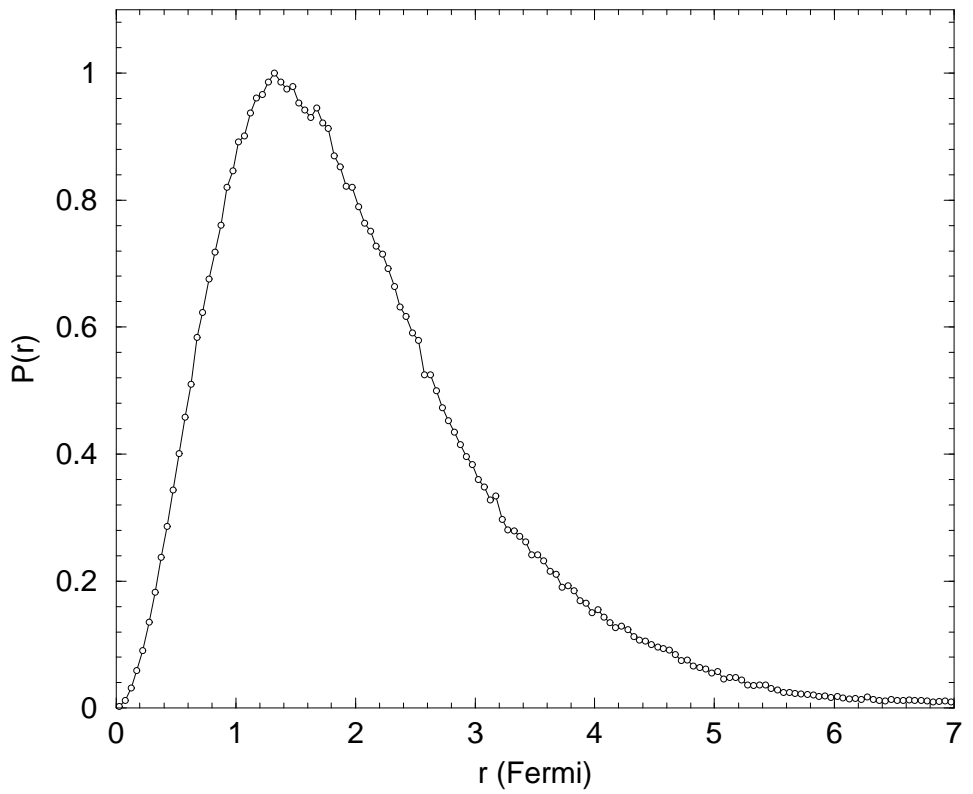


Figure 9: The radial probability distribution for the 2-body bound state is shown.

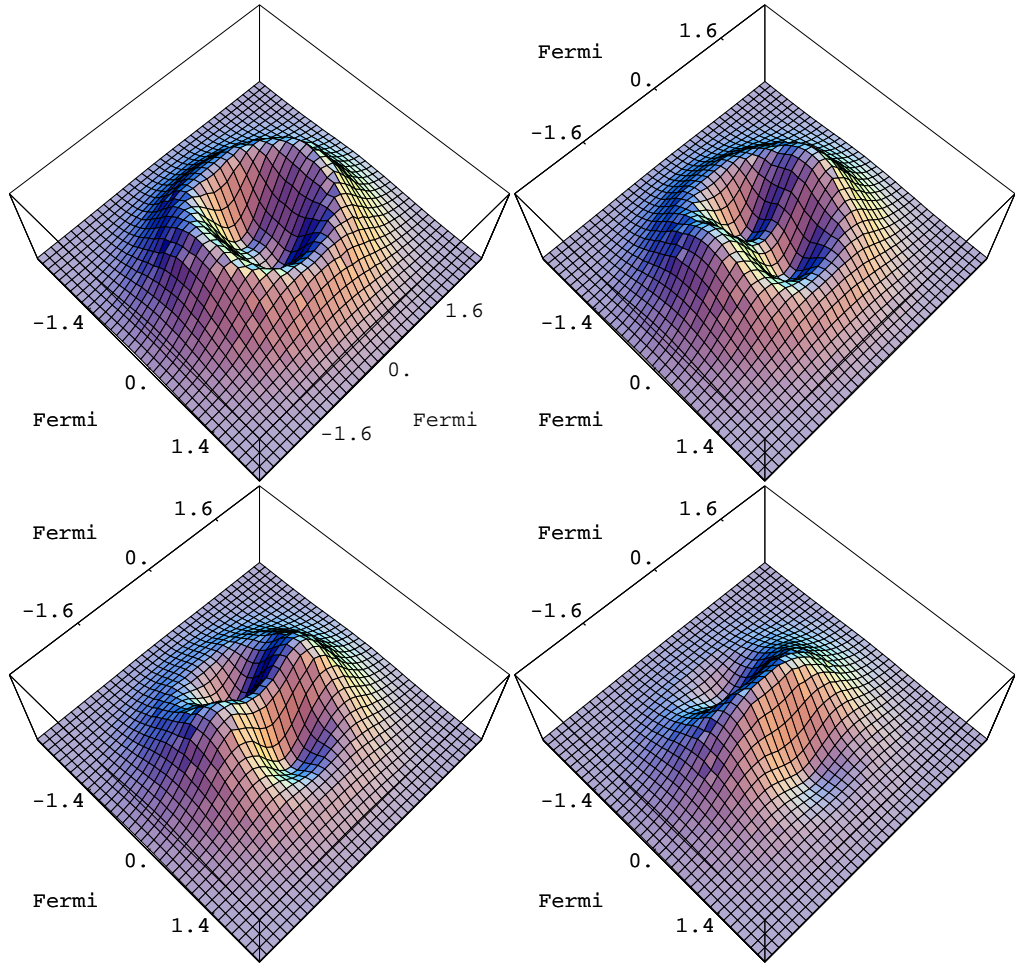


Figure 10: Evolution of the probability distribution for the 3rd particle is shown as the distance between the two fixed particles is increased. When the fixed particles are very close to each other the third particle sees them as a point particle (the upper left plot). As the fixed particles are separated from each other the third particle starts penetrating between them (2nd and 3rd plots), and as the two fixed particles are maximally separated the third particle spends most of its time in between the two fixed particles (the lower right plot).

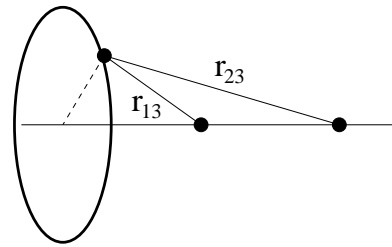


Figure 11: The radial probability distribution for the 3-body bound state shown in Fig. 10 includes the phase space factor represented by the ring in this figure. Distances  $r_{13}$ , and  $r_{23}$  are fixed on the ring and each point on the ring contribute to the probability distribution shown in Fig. 10.

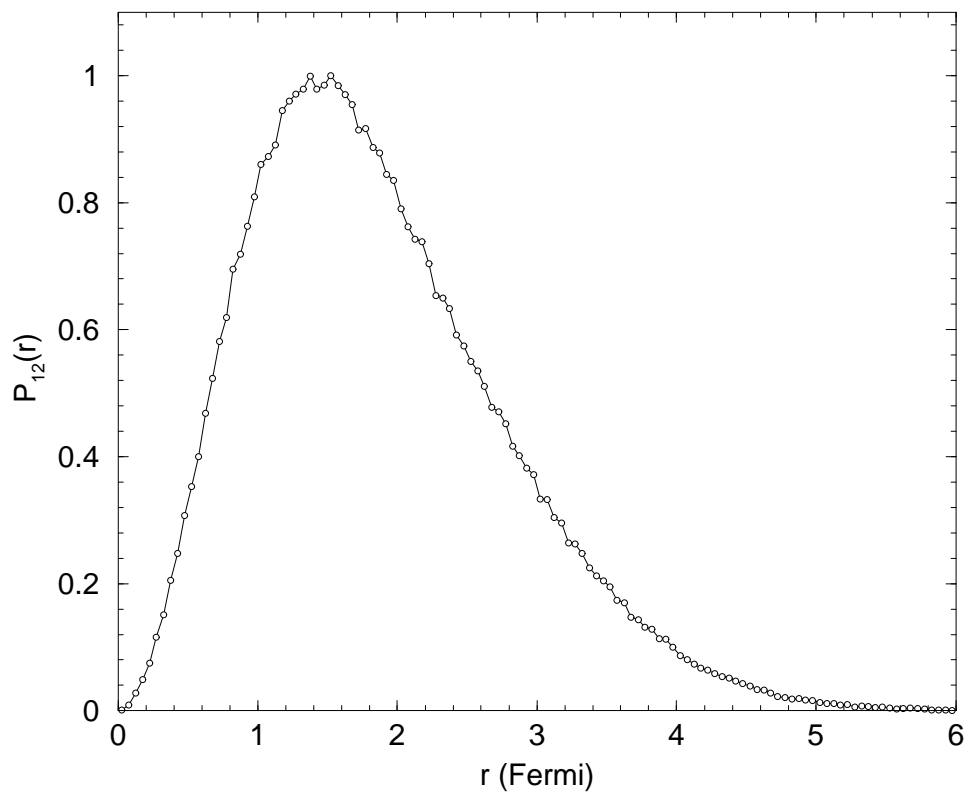


Figure 12: The radial *two-body* probability distribution  $P_{12}$  for the 3-body bound state is shown. This distribution is obtained by integrating out the location of the 3rd particle.